Article

Ab Initio Computations of O and AO as well as ReO$_2$, WO$_2$ and BO$_2$-Terminated ReO$_3$, WO$_3$, BaTiO$_3$, SrTiO$_3$ and BaZrO$_3$ (001) Surfaces

Roberts I. Eglitis [1,*], Juris Purans [1], Anatoli I. Popov [1], Dmitry Bocharov [1], Anastasiia Chekhovska [1] and Ran Jia [1,2,*]

[1] Institute of Solid State Physics, University of Latvia, 8 Kengaraga Street, LV1063 Riga, Latvia; purans@cfi.lu.lv (J.P.); popov@latnet.lv (A.I.P.); dmitrijs.bocarovs@cfi.lu.lv (D.B.); anastasiy101294@gmail.com (A.C.)

[2] Laboratory of Theoretical and Computation Chemistry, Institute of Theoretical Chemistry, Jilin University, Changchun 130023, China

* Correspondence: rieglitis@gmail.com (R.I.E.); jiaran@jlu.edu.cn (R.J.); Tel.: +371-26426703 (R.I.E.)

Abstract: We present and discuss the results of surface relaxation and rumpling computations for ReO$_3$, WO$_3$, SrTiO$_3$, BaTiO$_3$ and BaZrO$_3$ (001) surfaces employing a hybrid B3LYP or B3PW description of exchange and correlation. In particular, we perform the first B3LYP computations for O-terminated ReO$_3$ and WO$_3$ (001) surfaces. In most cases, according to our B3LYP or B3PW computations for both surface terminations BO$_2$- and O, AO-terminated ReO$_3$, WO$_3$, BaTiO$_3$, SrTiO$_3$ and BaZrO$_3$ (001) surface upper layer atoms shift downwards, towards the bulk, the second layer atoms shift upwards and the third layer atoms, again, shift downwards. Our ab initio computes that ReO$_3$, WO$_3$, BaTiO$_3$, SrTiO$_3$ and BaZrO$_3$ (001) surface Γ-Γ bandgaps are always smaller than their respective bulk Γ-Γ bandgaps. Our first principles compute that B-O atom chemical bond populations in the BaTiO$_3$, SrTiO$_3$ and BaZrO$_3$ perovskite bulk are always smaller than near their BO$_2$-terminated (001) surfaces. Just opposite, the Re-O and W-O chemical bond populations in the ReO$_3$ (0.212e) and WO$_3$ (0.142e) bulk are slightly larger than near the ReO$_2$ and WO$_2$-terminated ReO$_3$ as well as WO$_3$ (001) surfaces (0.170e and 0.108e, respectively).

Keywords: ab initio methods; (001) surfaces; ReO$_3$; WO$_3$; BaTiO$_3$; SrTiO$_3$; BaZrO$_3$

1. Introduction

Advanced (001) surfaces and interfaces in the ReO$_3$, WO$_3$ complex oxides as well as BaTiO$_3$, SrTiO$_3$ and BaZrO$_3$ perovskites are of paramount importance due to the numerous technological applications and great potential for fundamental research caused by their phase transitions [1–10]. Over the course of the last 25 years, the (001) surfaces of ReO$_3$ and WO$_3$, as well as BaTiO$_3$, SrTiO$_3$ and BaZrO$_3$ perovskites, have been broadly explored worldwide both from the theory and experimental sides [11–26]. All our ab initio computed BaTiO$_3$, SrTiO$_3$ and BaZrO$_3$ complex oxides belong to the commonly named ABO$_3$ perovskites. In our case, A is equal to Ba or Sr, whereas B denotes the Ti or Zr atoms [27]. Our computed materials ReO$_3$, WO$_3$, BaTiO$_3$, SrTiO$_3$ and BaZrO$_3$ have a huge number of applications in new and emerging technologies. For example, the novel trioxo-rhenium complex [ReO$_3$(phen)(H$_2$PO$_4$)]·H$_2$O has important antibacterial properties [28]. Tungsten oxide nanodots (WO$_{3-x}$) exhibit remarkable antibacterial capabilities [29]. Tungsten oxide and graphene oxide (WO$_3$-GO) nanocomposite is an excellent antibacterial as well as an anticancer agent [30]. BaTiO$_3$ may be used as an electrical insulator and a piezoelectric substance in different kinds of microphones as well as other transducers [31]. SrTiO$_3$ is an outstanding photocatalyst for the extremely important water splitting process [32,33]. BaZrO$_3$-based ceramic substances are widely used in protonic fuel cell applications [34–38] as well as in hydrogen separation membranes [39,40].

Along with its great technological potential [31,41], $BaTiO_3$ is also a marvellous material for fundamental research since it exhibits several phase transitions [42]. Namely, $BaTiO_3$ exists as one of four polymorphs [43,44] as a function of temperature. As the temperature lowers from high temperature to low temperature [43,44], the crystal symmetries of these four $BaTiO_3$ polymorphs are the cubic $BaTiO_3$ phase, tetragonal $BaTiO_3$ phase, orthorhombic $BaTiO_3$ phase and, finally, the rhombohedral $BaTiO_3$ phase [43,44]. Three of these four $BaTiO_3$ phases, tetragonal, orthorhombic and rhombohedral [43,44], display the ferroelectric effect [43,44]. It is worth noting that recently, the ab initio computations of the temperature effects on the structural, energetic, electronic as well as vibrational properties of four $BaTiO_3$ polymorphs by means of the quasi-harmonic approximations were carried out by Oliveira et al. [45]. The ab initio study of the stability between these four $BaTiO_3$ phases, performed by Oliveira et al. [45], breaks out into several contributions arising from the vibration of the lattice, electronic structure as well as volume expansion/contraction. This novel study by Oliveira et al. [45] was helpful in order to confirm the sequence of the $BaTiO_3$ phase transitions as cubic $\rightarrow$ tetragonal $\rightarrow$ orthorhombic $\rightarrow$ rhombohedral [45] and also its transition temperatures. In contrast to $BaTiO_3$, the $SrTiO_3$ and $BaTiO_3$ perovskites are so-called incipient ferroelectrics, and they exist only in their high symmetry cubic structure [46,47].

In our ab initio computations, we employed the standard cubic unit cells of $BaTiO_3$, $SrTiO_3$ and $BaZrO_3$ crystals containing five atoms [46,47]. The A-type ABO_3 perovskite atom in the cubic structure was positioned at the corner of the cube position. The ABO_3 perovskite A atom had the following fractional coordinates (0, 0, 0). The B-type ABO_3 perovskite atom in the cubic structure was positioned at the cube body center position. The B atom had the following fractional coordinates $1/2$, $1/2$, $1/2$). Lastly, at the ABO_3 perovskite, cubic phase face center positions were filled with three cubic ABO_3 perovskite O atoms. The three ABO_3 perovskite O atoms had the following fractional coordinates ($1/2$, $1/2$, 0), ($1/2$, 0, $1/2$) and (0, $1/2$, $1/2$) [48–51]. All three of our ab initio computed cubic ABO_3 perovskites ($BaTiO_3$, $SrTiO_3$ and $BaZrO_3$) had the $Pm\overline{3}m$ space group with the space group number 221. Additionally, the ReO_3 and WO_3 crystals at their cubic symmetry structure had exactly the same space group $Pm\overline{3}m$ with the same space group number 221. The only paramount difference between the $BaTiO_3$, $SrTiO_3$ and $BaZrO_3$ ABO_3 perovskites as well as ReO_3 and WO_3 crystals, which had exactly the same cubic symmetry structure, the same space group $Pm\overline{3}m$ and even the same space group number 221, was missing an A-type atom in the ReO_3 and WO_3 materials.

To the best of our knowledge, only a few ab initio computations up to now exist in the world of science, dealing with the ReO_2 or WO_2-terminated polar ReO_3 and WO_3 (001) surfaces [52–54]. It is worth noting that up to now there have been no ab initio computations performed in the world dealing with O-terminated polar ReO_3 or WO_3 (001) surfaces. For our ab initio computations, relevant experimental data [46,55–65] dealing with ReO_3, WO_3, $BaTiO_3$, $SrTiO_3$ and $PbTiO_3$ bulk crystals are collected in Table 1.

Table 1. Experimental details for ReO_3, WO_3, $BaTiO_3$, $SrTiO_3$ and $BaZrO_3$ crystals relevant to our ab initio computations. The experimental data include the crystal structure at room temperature (RT), bandgap values at RT, transition temperatures to cubic phase, as well as experimental lattice constants at cubic phase.

Crystal	Symmetry in RT	BandGap (Γ-Γ) (eV) in RT	Trans. T (K) to Cubic Phase	Exp. Latt. Con. (Å), Cubic Ph.
ReO_3	Cubic [55]	Unknown	Cubic from liquid helium T till 673 K	3.747 Å [61]
WO_3	Monoclinic [56]	3.74 eV [57]	Unknown	3.71–3.75 Å [62]
$BaTiO_3$	Tetragonal ↔ orthorhombic (278 K)	3.38 eV ($\parallel$ c); 3.27 eV ($\perp$ c) [58]	403 K [45]	4.004 Å—474 K [63]
$SrTiO_3$	Cubic	3.75 eV [59]	110 K [45]	3.898 Å—110 K [64]
$BaZrO_3$	Cubic	5.3 eV [60]	Cubic, all T	4.199 Å RT [65]

The perfect cubic structure for the ReO_3 conducting oxide [55] is stable at all temperature ranges starting from room temperature. The crystal structure of tungsten trioxide (WO_3) [56] depends on the temperature. WO_3 has tetragonal symmetry if the temperature is above 740 °C. WO_3 is orthorhombic [56] at the temperature range from 330 °C to 740 °C. WO_3 is monoclinic [56] at the temperature range from 17 °C to 330 °C. Finally, WO_3 is triclinic [56] at the temperature range from -50 °C to 17 °C. It is worth noting that the most common structure for WO_3 is monoclinic. The space group for the WO_3 monoclinic structure is $P2_{1/n}$. The experimentally measured WO_3 (Γ-Γ) bandgap is equal to 3.74 eV [57]. In the $BaTiO_3$ perovskite matrix, according to the experimental measurements performed by Wemple, the room temperature (RT) bandgaps are equal to 3.38 eV and 3.27 eV [58] for the light polarized parallel and perpendicular to the ferroelectric axis *c*. The experimental $SrTiO_3$ Γ-Γ bandgap, according to measurements by Benthem et al. [59], is equal to 3.75 eV (Table 1). Finally, the experimental $BaZrO_3$ Γ-Γ bandgap, according to experiments performed by Robertson, is equal to 5.3 eV [60] (Table 1). ReO_3 is cubic at all temperatures, starting from liquid helium temperature to 673 K. The experimentally measured ReO_3, WO_3, $BaTiO_3$, $SrTiO_3$ and $BaZrO_3$ bulk lattice constants in cubic crystal structures are listed by us in Table 1. The objective of our contribution was to carry out the first ab initio computations for polar O-terminated ReO_3 and WO_3 (001) surfaces. We compared our ab initio computation results for polar ReO_3 and WO_3 as well as neutral $BaTiO_3$, $SrTiO_3$ and $BaZrO_3$ perovskite (001) surfaces and pointed out systematic tendencies in our performed computations in a way that is comfortably approachable for a broad audience of readers worldwide.

2. Computation Methods and Materials

We performed our forefront ab initio computations for the ReO_3, WO_3, $BaTiO_3$, $SrTiO_3$ and $BaZrO_3$ bulk and their (001) surfaces by means of the hybrid B3PW [66,67] or B3LYP [68] exchange-correlation functionals. Both these B3PW [66,67] as well as B3LYP [68] hybrid exchange-correlation functionals are implemented into the very famous, world-class computational package CRYSTAL [69], developed by Torino University, Italy. The computational package CRYSTAL [69] utilizes 2-D isolated slab representation for the (001) surface structure first principles computations. We performed the reciprocal space integration in our first principles computations for ReO_3, WO_3, $BaTiO_3$, $SrTiO_3$ and $BaZrO_3$ matrixes. Namely, we integrated the Brillouin zone employing the $8 \times 8 \times 8$ times expanded Pack–Monkhorst [70] net for the bulk ab initio computations as well as $8 \times 8 \times 1$ times enlargement for the (001) surface ab initio computations of these materials. In order to achieve the high accuracy of our computations, sufficiently large tolerances of 7, 8, 7, 7 and 14 were used by us for the Coulomb overlap, Coulomb penetration, exchange overlap, the first exchange pseudo-overlap as well as for the second exchange pseudo-overlap, respectively. With

the goal of detecting the performance of various non-identical methods, we computed the bulk Γ-Γ bandgaps for ReO_3, WO_3, $BaTiO_3$, $SrTiO_3$ and $BaZrO_3$ matrixes (Table 2 and Figure 1) and compared our ab initio computation results with the available experimental data [14,59,60,71–76].

Table 2. $BaTiO_3$, $SrTiO_3$, $BaZrO_3$, MgF_2 as well as CaF_2 (Γ-Γ) bulk bandgaps (in eV) ab initio computed by means of various methods [14,71–74]. Available experimental data for bulk (Γ-Γ) bandgaps (in eV) are listed for comparison purpose [59,60,72,75,76].

Approach	$BaTiO_3$	$SrTiO_3$	$BaZrO_3$	MgF_2	CaF_2
HF	11.73	12.33	12.96	19.65	20.77
B3PW	3.55	3.96	4.93	9.48	10.96
B3LYP	3.49	3.89	4.79	9.42	10.85
PWGGA	1.97	2.31	3.24	6.94	8.51
Experiment	3.2 [72]	3.75 [59]	5.3 [60]	13.0 [76]	12.1 [75]
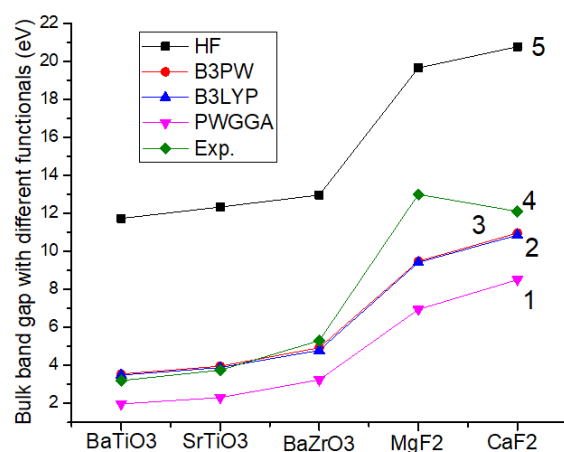
Figure 1. Ab initio computed and experimentally studied bulk Γ-Γ bandgaps (in eV) for $BaTiO_3$, $SrTiO_3$, $BaZrO_3$, MgF_2 and CaF_2 crystals obtained by means of different methods: (1) PWGGA; (2) B3LYP; (3) B3PW; (4) Experiment; (5) HF.

As it is possible to see from Table 2 and Figure 1, the Hartree–Fock (HF) [77,78] method always, for all computed materials, significantly overestimates the Γ-Γ bandgap. For example, our ab initio computed $BaTiO_3$ (Γ-Γ) bulk bandgap is overestimated by 3.67 times with respect to the experimental $BaTiO_3$ bulk Γ-Γ bandgap values (Table 2). Additionally, our ab initio computed $SrTiO_3$ bulk Γ-Γ bandgap is overestimated by 3.29 times regarding the experimental $SrTiO_3$ bulk Γ-Γ bandgap value (Table 2). In our density functional theory (DFT) computations, we used the local density approximation (LDA) with the Dirac–Slater exchange [79] as well as the Vosko–Wilk–Nusair correlation [80] energy functionals and a set of GGA exchange and correlation functionals as suggested by Perdew and Wang (PWGGA) [66,67]. On another side, the ab initio computed Γ-Γ bulk bandgaps for all five materials using the PWGGA are always considerably underestimated with respect to the experimental bulk Γ-Γ bandgap values (Table 2 and Figure 1). For example, our ab initio PWGGA computed MgF_2 bulk Γ-Γ bandgap value (6.94 eV) is 1.97 times underestimated with respect to the experimental MgF_2 Γ-Γ bulk bandgap value equal to (13.0 eV) [76] (Figure 1 and Table 2). As we can see from Table 2 and Figure 1, the hybrid exchange-correlation functionals B3PW and B3LYP always allow us to achieve the best possible agreement between the ab initio computed as well as experimental bulk Γ-Γ bandgaps for all five of our first principles computed materials $BaTiO_3$, $SrTiO_3$, $BaZrO_3$, MgF_2 as well as CaF_2. The main reason for such a good agreement is that the hybrid B3LYP and B3PW functionals include a portion of exact exchange energy density from the HF theory (20%),

while the rest of the exchange-correlation part is a mixture of various approaches (both exchange and correlation). This is the key reason why we performed all our future bulk as well as (001) surface ab initio computations by means of the B3PW or B3LYP hybrid exchange-correlation functionals (Table 2 and Figure 1).

With an aim to ab initio compute the TiO_2-terminated $BaTiO_3$, $SrTiO_3$ and ZrO_2-terminated $BaZrO_3$ (001) surfaces, we selected nine-layer, mirror-symmetrical (001) slabs. They consisted of neutral and alternating $TiO_2(ZrO_2)$ or AO layers (Figure 2). These slabs were positioned perpendicular to the axis *z*. Our generated nine-layer slab, used by us in ABO_3 perovskite (001) surface ab initio computations, was terminated from both sides by the TiO_2-terminated planes for $BaTiO_3$ and $SrTiO_3$ perovskites as well as by ZrO_2-terminated planes for $BaZrO_3$ perovskite (Figure 2). Accordingly, our in ab initio computations employed the (001) surface model for the BO_2-terminated ABO_3 perovskites and the nine-layer slab consisted of a 23-atom supercell. Our ab initio computed ABO_3 perovskite BO_2-terminated (001) slab was non-stoichiometric (Figure 2), and it had the following chemical equation $A_4B_5O_{14}$. With the objective to directly compare the properties of three perovskites ($BaTiO_3$, $SrTiO_3$ and $BaZrO_3$) as well as ReO_3 and WO_3 materials under the same conditions and, as much as possible, to reduce the computational time, we only investigated the high symmetry ($Pm\overline{3}m$) cubic phases of these five materials. In our surface structure B3LYP and B3PW first principles computations, we allowed the atoms of the upper two or three surface layers to only relax along the *z*-axis since the (001) surfaces of the perfect cubic crystals, due to symmetry restrictions, do not have any forces acting along the other *x*- or *y*-axes. We optimized the (001) surface atom atomic coordinated through the slab total energy minimization. For this purpose, we employed our own computer code, which implements [81] conjugated gradients optimization technique with numerical computation of derivatives [81].
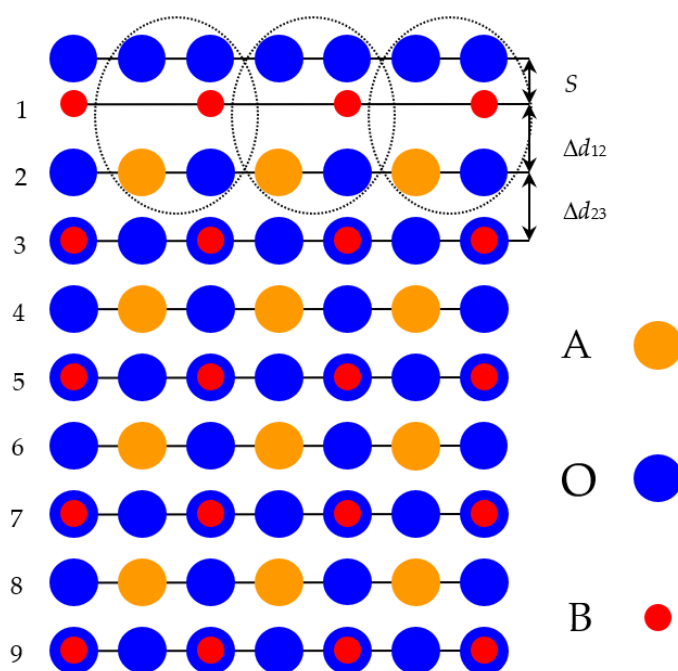
Figure 2. Side view of the BO_2-terminated ABO_3 perovskite (001) surface slab containing 9 layers as well as the definitions of the surface rumpling *s* and the near-surface interplane distances Δd_{ij}.

Just opposite to our ab initio computed neutral $BaTiO_3$, $SrTiO_3$ and $BaZrO_3$ (001) surfaces, which are built up from the neutral BO_2 or AO layers (Figure 2), the WO_2 or ReO_2-terminated polar WO_3 or ReO_3 (001) surfaces were formed from charged (Figure 3) WO_2 (ReO_2) or O layers. This is much more demanding to compute at the ab initio level for the polar WO_2 or ReO_2-terminated WO_3 or ReO_3 (001) surfaces (Figure 3) than the neutral (Figure 2) ABO_3 perovskite BO_2-terminated (001) surfaces [8,52,82–84]. For example, in our

ab initio computations, the ReO_2-terminated polar ReO_3 (001) surface consisted of nine alternating ReO_2 or O layers (Figure 3). This means that this ReO_2-terminated ReO_3 polar (001) surface contained 19 atoms and had the chemical equation Re_5O_{14}.
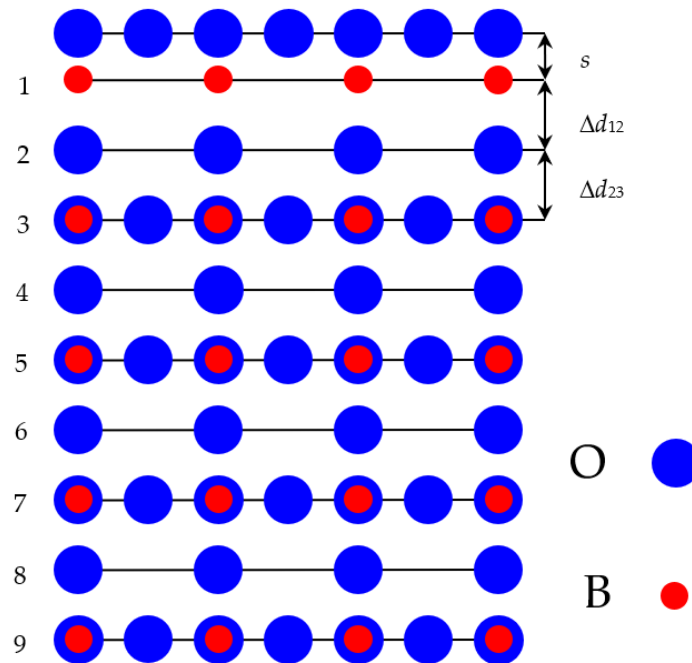

Figure 3. Side view of the BO_2-terminated ReO_3 or WO_3 (001) surface slab containing 9 layers as well as the definitions of the surface rumpling s and the near-surface interplane distances Δd_{ij}.

In our ab initio computations, we employed the neutral atomic basis sets for all three atoms entering the WO_3 and ReO_3 crystals. Namely, we used the neutral W atom basis set from the reference [85] for the W atom. Additionally, for the Re atom, we used the neutral atom basis set from the reference [69]. Finally, for the O atom, again, we used the neutral O atom basis set, developed by Piskunov et al., from reference [71]. Using the neutral atomic basis sets for all three Re, W and O atoms, we determined in our ab initio computations that both ReO_2 and WO_2-terminated ReO_3 and WO_3 (001) surfaces have a total charge of our employed nine-layer slab equal to zero. In our ab initio computations, we utilized the well-known classical Mulliken population analysis for the description of the ReO_3, WO_3, $BaTiO_3$, $SrTiO_3$ and $BaZrO_3$ effective atomic charges q and also their chemical bond populations P [86–89].

For our ab initio computations of AO-terminated $BaTiO_3$, $SrTiO_3$ and $BaZrO_3$ (001) neutral surfaces, we used, from both sides, AO-terminated mirror-symmetrical slabs containing nine alternating AO and BO_2 layers (Figure 4). These AO-terminated ABO_3 perovskite (001) nine-layer slabs consisted of a supercell containing 22 atoms (Figure 4). They were non-stoichiometric, and they had the following unit cell equation $A_5B_4O_{13}$ (Figure 4). The only striking difference between the AO-terminated $BaTiO_3$, $SrTiO_3$ and $BaZrO_3$ (001) slabs (Figure 4) and O-terminated ReO_3 and WO_3 slabs was the missing O atom in the ReO_3 and WO_3 (001) slabs (Figure 5). Thereby, the O-terminated ReO_3 and WO_3 nine-layer (001) slabs consisted of alternating O-BO_2-O-BO_2-O-BO_2-O-BO_2-O layers (Figure 5). They contained 17 atoms and had the following unit cell equation B_4O_{13} (Figure 5).
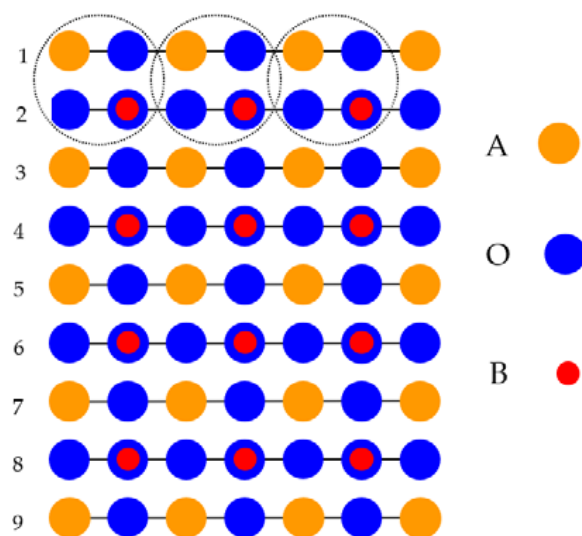
Figure 4. Side view of the AO-terminated ABO_3 perovskite 9 layers containing (001) surface.
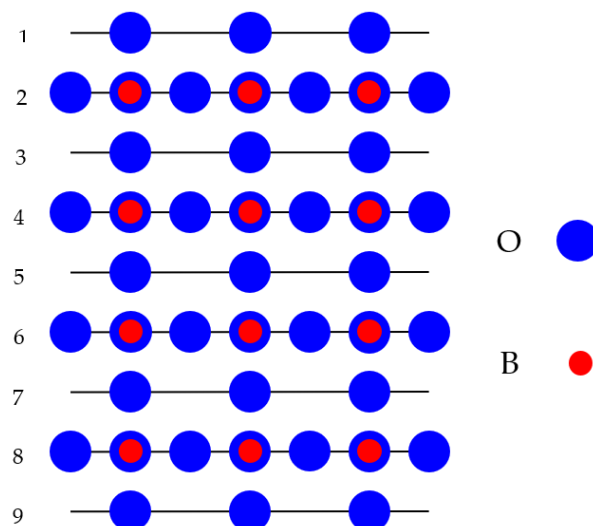

Figure 5. Side view of the O-terminated ReO_3 and WO_3 (001) surface containing nine-layer slabs.

3. Ab Initio Computation Results for ReO_3, WO_3, $BaTiO_3$, $SrTiO_3$ and $BaZrO_3$ Bulk Properties

As an opening of our first principles computations, by means of the B3LYP or B3PW hybrid exchange-correlation functionals, we computed the ReO_3, WO_3, $BaTiO_3$, $SrTiO_3$ and $BaZrO_3$ bulk lattice constants [52–54,90–93]. It is worth noting that we performed all our ab initio computations by B3LYP hybrid exchange-correlation functional B3LYP for ReO_3 and WO_3 matrixes as well as by B3PW hybrid exchange-correlation functional for $BaTiO_3$, $SrTiO_3$ and $BaZrO_3$ perovskites. Our ab initio computed bulk lattice constants for ReO_3 (3.758 Å), WO_3 (3.775 Å), $BaTiO_3$ (4.008 Å), $SrTiO_3$ (3.904 Å) and $BaZrO_3$ (4.234 Å) perovskites are in a fine agreement with the obtained experimental measurements (Table 1). For example, our ab initio B3LYP computed ReO_3 bulk lattice constant (3.758 Å) is only overestimated by approximately 0.29% with respect to the experimental ReO_3 bulk lattice constant equal to 3.747 Å (Table 1). Additionally, our ab initio B3PW computed $BaTiO_3$ bulk lattice constant (4.008 Å) is almost in a perfect agreement with the experimentally measured $BaTiO_3$ bulk lattice constant (4.004 Å) (Table 1).

As we can see from Table 3, our ab initio computed atomic charges for all atoms are considerably smaller than the generally accepted classical ionic charges in ABO_3 perovskites for Ba or Sr atoms ($+2e$), for Ti or Zr atoms ($+4e$), or for O atoms ($-2e$). Additionally, our

ab initio computed Re and W atom effective charges in ReO_3 or WO_3 materials (+2.382e or +3.095e, respectively) are considerably smaller than the Re or W classical ionic charges equal to (+6e). It is worth noting that the absolute values of O atom charges in the ABO_3 perovskites $BaTiO_3$, $SrTiO_3$ and $BaZrO_3$ (−1.388e, −1.407e, and −1.316e, respectively) are always larger than the absolute values of O atom charges in the ReO_3 or WO_3 crystals (−0.794e or −1.032e, respectively). Just opposite, our ab initio computed chemical bond populations between the Re and O as well as W and O atoms in the ReO_3 and WO_3 materials (Table 3) (+0.212e and +0.142e, respectively) are always considerably larger than the respective B-O atom chemical bond populations in the $BaTiO_3$, $SrTiO_3$ and $BaZrO_3$ perovskites (+0.098e, +0.088e and +0.108e, respectively).

Table 3. Our ab initio B3LYP or B3PW computed ReO_3, WO_3, $BaTiO_3$, $SrTiO_3$ and $BaZrO_3$ bulk crystal effective atomic charges Q (in e) as well as bond populations P (in e) between the atoms.

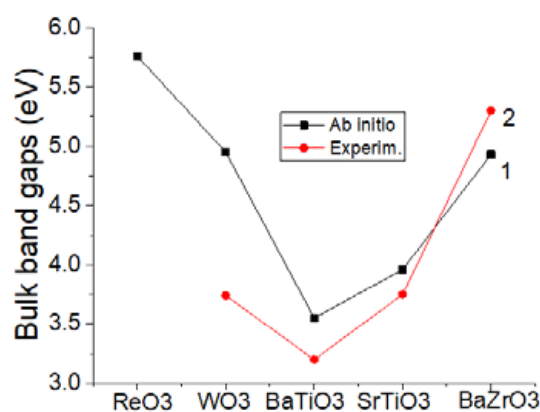| Crystal		ReO_3	WO_3	$BaTiO_3$	$SrTiO_3$	$BaZrO_3$
Atom	**Property**	**B3LYP**	**B3LYP**	**B3PW**	**B3PW**	**B3PW**
A	Q	-	-	+1.797	+1.871	+1.815
	P	-	-	−0.034	−0.010	−0.012
O	Q	−0.794	−1.032	−1.388	−1.407	−1.316
	P	+0.212	+0.142	+0.098	+0.088	+0.108
B	Q	+2.382	+3.095	+2.367	+2.351	+2.134

As a next step, by means of B3LYP or B3PW (Table 4 and Figure 6) hybrid exchange-correlation functionals, at the ab initio level, we computed the ReO_3, WO_3, $BaTiO_3$, $SrTiO_3$ and $BaZrO_3$ bulk Γ-Γ bandgaps. As we can see from Table 4 and Figure 6, our B3LYP computed ReO_3 bulk Γ-Γ bandgap is equal to 5.76 eV. This is a theoretical prediction since, to the best of our knowledge, there is no experimental bandgap yet detected for the ReO_3 matrix at Γ-point. Our computed WO_3 bulk Γ-Γ bandgap (4.95 eV) by 1.21 eV exceeds the WO_3 experimentally detected [56] bulk Γ-Γ bandgap (Table 4). Determined by means of the B3PW hybrid exchange-correlation functional ab initio, our computed $BaTiO_3$ (3.55 eV), $SrTiO_3$ (3.96 eV) and $BaZrO_3$ (4.93 eV) bulk Γ-Γ bandgaps are in a fair agreement with the experimentally measured bulk Γ-Γ bandgaps for $BaTiO_3$, $SrTiO_3$ and $BaZrO_3$ perovskites (3.2 eV, 3.75 eV and 5.3 eV, respectively) (Table 4 and Figure 6).

Table 4. Our ab initio B3LYP or B3PW computed ReO_3, WO_3, $BaTiO_3$, $SrTiO_3$ and $BaZrO_3$ bulk Γ-Γ bandgaps (in eV). Experimentally measured Γ-Γ bulk bandgaps (in eV) are listed for comparison purposes.

Material	Theoretical Γ-Γ Bulk Gap (eV)	Experimental Γ-Γ Bulk Gap (eV)
ReO_3	5.76 eV (B3LYP)	Unknown
WO_3	4.95 eV (B3LYP)	3.74 eV [57]
$BaTiO_3$	3.55 eV (B3PW)	3.2 eV [72]
$SrTiO_3$	3.96 eV (B3PW)	3.75 eV [59]
$BaZrO_3$	4.93 eV (B3PW)	5.3 eV [60]

Figure 6. Ab initio computed (1) as well as experimentally measured (2) bulk Γ-Γ bandgaps (in eV) for ReO_3, WO_3, $BaTiO_3$, $SrTiO_3$ and $BaZrO_3$.

4. Ab Initio Computation Results for the BO_2 and O-Terminated ReO_3, WO_3, $BaTiO_3$, $SrTiO_3$ and $BaZrO_3$ (001) Surfaces

As we can see from our ab initio computation results for ReO_2 and WO_2-terminated ReO_3 and WO_3, as well as BO_2-terminated $BaTiO_3$, $SrTiO_3$ and $BaZrO_3$ (001) surfaces, collected in Table 5, for all five our computed materials ReO_3, WO_3, $BaTiO_3$, $SrTiO_3$ and $BaZrO_3$, the upper layer atoms relax inwards, in the direction towards the bulk (Table 5). The only exception from this systematic trend is the upward shift of the WO_2-terminated WO_3 (001) surface upper layer O atom by 0.42% of a_0 (Table 5). Just opposite, all second layer atoms relax upwards, with the single exception of the ReO_2-terminated ReO_3 (001) surface second layer O atom, which relaxes inwards by 0.32% of the ReO_3 cubic lattice constant a_0 (Table 5). Again, all third layer ReO_2 and WO_2-terminated ReO_3 and WO_3, as well as ZrO_2-terminated $BaZrO_3$ (001) surface atoms, relax inwards (Table 5). It is worth noting that for all our calculated ReO_2 and WO_2-terminated ReO_3 and WO_3 as well as BO_2-terminated $BaTiO_3$, $SrTiO_3$ and $BaZrO_3$ perovskite (001) surfaces, in all three layers the metal atom displacement magnitudes are always larger than the O atom displacements (Table 5).

Table 5. ReO_2 and WO_2-terminated ReO_3 and WO_3 as well as BO_2-terminated $BaTiO_3$, $SrTiO_3$ and $BaZrO_3$ perovskite (001) surface upper three-layer atom shifts (in % of the bulk lattice constant a_0).

Computed (001) Surf.		ReO_3	WO_3	$BaTiO_3$	$SrTiO_3$	$BaZrO_3$
Layer	**Atom**	ReO_2-Ter.	WO_2-Ter.	TiO_2-Ter.	TiO_2-Ter.	ZrO_2-Ter.
1	B	−3.19	−2.07	−3.08	−2.25	−1.79
	O	−1.17	+0.42	−0.35	−0.13	−1.70
2	A	No atom	No atom	+2.51	+3.55	+1.94
	O	−0.32	+0.11	+0.38	+0.57	+0.85
3	B	−0.17	−0.01	-	-	−0.03
	O	−0.11	0.00	-	-	0.00

It is worth noting that we are the first in the world to perform ab initio computations for O-terminated ReO_3 and WO_3 (001) surfaces (Table 6). As we can see from our ab initio computation results for O-terminated ReO_3, WO_3, $BaTiO_3$, $SrTiO_3$ and $BaZrO_3$ (001) surfaces, all upper-layer atoms relax inwards (Table 6). The only single exception from this systematic trend is the upwards relaxation of the SrO-terminated $SrTiO_3$ (001) surface upper layer O atom by +0.84% (Table 6) of the $SrTiO_3$ bulk lattice constant a_0. In contrast, almost all second layer atoms relax upwards. The only two exceptions are the inward relaxation of O-terminated ReO_3 and WO_3 (001) second layer O atoms by (−0.53 and −0.11% of a_0,

respectively) (Table 6). Finally, all our ab initio calculated third layer atoms relax inwards, towards the bulk. It is worth noting that for both upper O-terminated ReO_3, WO_3, $BaTiO_3$, $SrTiO_3$ and $BaZrO_3$ (001) surface layers, the metal atom displacement magnitudes are always larger than the O atom relaxation shifts (Table 6).

Table 6. O-terminated ReO_3, WO_3, $BaTiO_3$, $SrTiO_3$ and $BaZrO_3$ (001) surface upper three-layer atom shifts (in % of the bulk lattice constant a_0).

Computed (001) Surf.		ReO_3	WO_3	$BaTiO_3$	$SrTiO_3$	$BaZrO_3$
Layer	Atom	O-Termin.	O-Termin.	BaO-Ter.	SrO-Ter.	BaO-Ter.
1	A	No atom	No atom	−1.99	−4.84	−4.30
	O	−3.73	−4.24	−0.63	+0.84	−1.23
2	B	+2.71	+2.65	+1.74	+1.75	+0.47
	O	−0.53	−0.11	+1.40	+0.77	+0.18
3	A	No atom	No atom	-	-	−0.01
	O	−0.44	−0.48	-	-	−0.14

Comparison of our ab initio calculation results with other calculations as well as available experimental data for SrO-terminated $SrTiO_3$ (001) surface [94–98] are listed in Table 7. As we can see from Table 7, our ab initio B3PW computed surface rumpling amplitudes s for SrO-terminated $SrTiO_3$ (001) surfaces (+5.66% of a_0) are in a qualitative agreement with other computation results ranging from (+5.8% of a_0) to (+8.2% of a_0) as well as in a qualitative agreement with available experimental data (Table 7). Additionally, our ab initio investigation calculated that changes in the interlayer distances Δd_{12} and Δd_{23} are in qualitative agreement with other calculation results and most experiments (Table 7). Unfortunately, our computed changes in interlayer distances Δd_{12} disagree with the RHEED experiment (Table 7), but our computed changes in interlayer distance Δd_{23} disagree with the SXRD experiment (Table 7). Nevertheless, since the LEED, RHEED and SXRD experiments do not always agree with each other, even with respect to signs, we can not take these LEED, RHEED and SXRD experiments (Table 7) too seriously.

Table 7. Surface rumpling s and relative displacements Δd_{ij} for the 3 near-surface planes of SrO-terminated $SrTiO_3$ (001) surface [94–98].

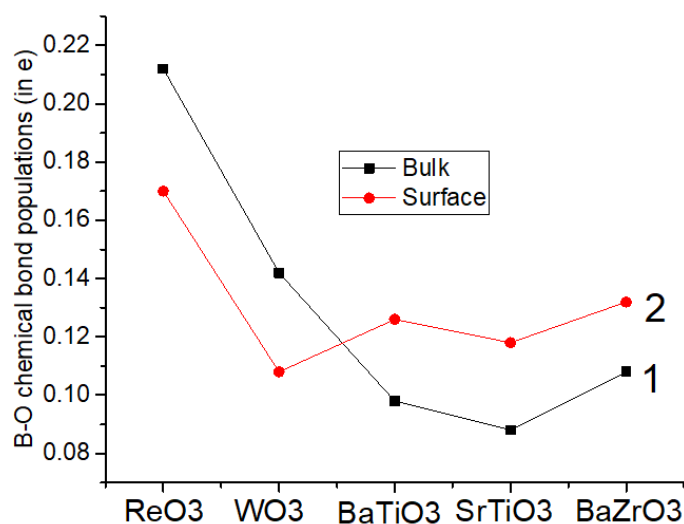| SrO-Terminated $SrTiO_3$ (001) Surface			
	s	Δd_{12}	Δd_{23}
Our B3PW results	+5.66	−6.58	+1.75
Ab initio [94]	+5.8	−6.9	+2.4
Ab initio [95]	+7.7	−8.6	+3.3
Shell model [48]	+8.2	−8.6	+3.0
LEED exp. [96]	4.1 ± 2	−5 ± 1	2 ± 1
RHEED exp. [97]	4.1	2.6	1.3
SXRD exp. [98]	1.3 ± 12.1	−0.3 ± 3.6	−6.7 ± 2.8

Our ab initio computed that B-O atom chemical bond populations in the $BaTiO_3$, $SrTiO_3$ and $BaZrO_3$ perovskite bulk (Table 8 and Figure 7) are always smaller than near their BO_2-terminated (001) surfaces. Just opposite, the Re-O and W-O chemical bond populations in the ReO_3 (0.212e) and WO_3 (0.142e) bulk (Table 8 and Figure 7) are slightly larger than near the ReO_2 and WO_2-terminated ReO_3 as well as WO_3 (001) surfaces (0.170e and 0.108e, respectively) (Table 8 and Figure 7). Nevertheless, the largest chemical bond populations in the ReO_3 and WO_3 matrixes are among the upper layer Re atom and the

second layer O atom (0.262*e*) as well as among the upper layer W atom and the second layer O atom (0.278*e*).

Table 8. Our ab initio computed Re-O, W-O and B-O chemical bond populations (in *e*) for the ReO_3, WO_3, $BaTiO_3$, $SrTiO_3$ and $BaZrO_3$ crystal bulk as well as their ReO_2-, WO_2- and BO_2-terminated ReO_3, WO_3, $BaTiO_3$, $SrTiO_3$ and $BaZrO_3$ (001) surfaces.

| Material	Functional	Re-O, W-O and B-O Chemical Bond Populations (in *e*)	
		Bulk	**ReO_2, WO_2, BO_2-Term. (001) Surfaces**
ReO_3	B3LYP	0.212	0.170
WO_3	B3LYP	0.142	0.108
$BaTiO_3$	B3PW	0.098	0.126
$SrTiO_3$	B3PW	0.088	0.118
$BaZrO_3$	B3PW	0.108	0.132

Figure 7. Our ab initio computed Re-O, W-O and B-O chemical bond populations (in *e*) for the ReO_3, WO_3, $BaTiO_3$, $SrTiO_3$ and $BaZrO_3$ crystal bulk (line 1) as well as their ReO_2-, WO_2- and BO_2-terminated ReO_3, WO_3, $BaTiO_3$, $SrTiO_3$ and $BaZrO_3$ (001) surfaces (line 2).

According to our ab initio computations, the Γ-Γ bandgaps near the BO_2, AO, or O-terminated ReO_3, WO_3, $BaTiO_3$, $SrTiO_3$ and $BaZrO_3$ (001) surfaces are always reduced with respect to their relevant bulk Γ-Γ bandgaps (Table 9 and Figure 8). Experimental data, where available, for the bulk Γ-Γ bandgaps are listed for comparison purposes (Figure 8 and Table 9). As we can see from Table 9 and Figure 8, for ReO_3 and WO_3 crystals, our ab initio computed Γ-Γ bandgaps near their O and especially ReO_2 and WO_2-terminated (001) surfaces are much more strongly reduced with respect to their bulk Γ-Γ bandgap values, than near the BO_2 and AO-terminated $BaTiO_3$, $SrTiO_3$ and $BaZrO_3$ perovskite (001) surfaces. For example, TiO_2 (3.95 eV) and SrO-terminated (3.72 eV) $SrTiO_3$ (001) surface Γ-Γ bandgaps are reduced only by (0.01 and 0.24 eV, respectively) regarding their bulk Γ-Γ bandgap value of 3.96 eV (Table 9 and Figure 8).

Table 9. Our ab initio computed bulk Γ-Γ bandgaps as well as Γ-Γ bandgaps near the BO$_2$ or AO-terminated ReO$_3$, WO$_3$, BaTiO$_3$, SrTiO$_3$ and BaZrO$_3$ (001) surfaces (in eV). Experimental bulk Γ-Γ bandgaps are listed for comparison purposes.

Material	Functional	Bulk (Γ-Γ)	Exp. (Γ-Γ)	BO$_2$-T. (001)	AO-T. (001)
ReO$_3$	B3LYP	5.76	No data	0.22	1.86
WO$_3$	B3LYP	4.95	3.74	1.16	1.98
BaTiO$_3$	B3PW	3.55	3.2	2.96	3.49
SrTiO$_3$	B3PW	3.96	3.75	3.95	3.72
BaZrO$_3$	B3PW	4.93	5.3	4.48	4.82
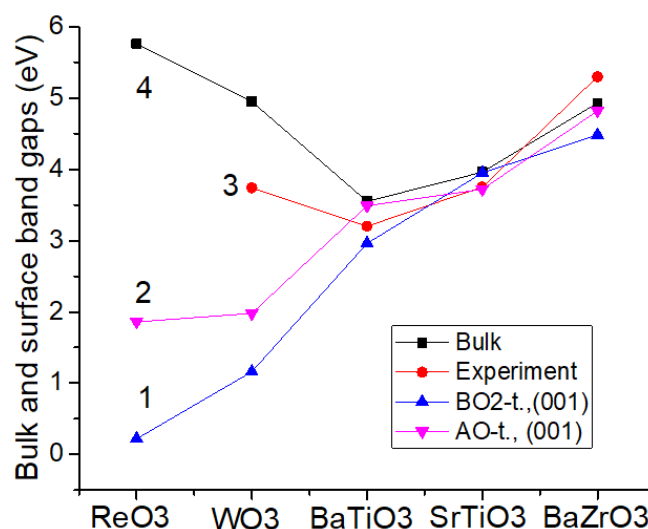
Figure 8. Our ab initio computed ReO$_3$, WO$_3$, BaTiO$_3$, SrTiO$_3$ and BaZrO$_3$ bulk Γ-Γ bandgaps (in eV) (line 4), experimental bulk Γ-Γ bandgaps (line 3), AO-terminated (001) surface bandgaps at Γ-point (line 2) as well as BO$_2$-terminated (001) surface bandgaps at Γ-point (line 1).

5. Conclusions

According to our ab initio computation results for BO$_2$, AO and O-terminated ReO$_3$, WO$_3$, SrTiO$_3$, BaTiO$_3$ and BaZrO$_3$ (001) surfaces, in most cases, the upper surface layer atoms relax inwards towards the bulk. The second surface layer atoms, again, in most cases, relax upwards, while the third layer atoms, again, relax inwards.

Our ab initio computation results for SrO-terminated SrTiO$_3$ (001) in most cases are in a fair agreement with previous calculation results and available experimental data. It is worth noting that our ab initio calculated interlayer distance Δd_{12} disagrees with the RHEED experiment (Table 7) with respect to the sign. Nevertheless, since the RHEED experiment also disagrees with the LEED and SXRD experiments, we can probably not take this available RHEED experiment [97] too seriously (Table 7).

According to our ab initio computations, the Γ-Γ bandgaps near the BO$_2$, AO or O-terminated ReO$_3$, WO$_3$, BaTiO$_3$, SrTiO$_3$ and BaZrO$_3$ (001) surfaces are always reduced with respect to their relevant bulk Γ-Γ bandgaps.

Our ab initio computed B-O atom chemical bond populations in the BaTiO$_3$, SrTiO$_3$ and BaZrO$_3$ perovskite bulk are always smaller than near their BO$_2$-terminated (001) surfaces. Just opposite, the Re-O and W-O chemical bond populations in the ReO$_3$ (0.212e) and WO$_3$ (0.142e) bulk are slightly larger than near the ReO$_2$ and WO$_2$-terminated ReO$_3$ as well as WO$_3$ (001) surfaces (0.170e and 0.108e, respectively). Nevertheless, the largest chemical bond populations in the ReO$_3$ and WO$_3$ matrixes are among the upper layer Re atom and the second layer O atom (0.262e) as well as among the upper layer W atom and the second layer O atom (0.278e).

References

1. Eglitis, R.I.; Vanderbilt, D. *Ab initio* calculations of the atomic and electronic structure of $CaTiO_3$ (001) and (011) surfaces. *Phys. Rev. B* **2008**, *78*, 155420. [CrossRef]

2. Erdman, N.; Warschkow, O.; Asta, M.; Poeppelmeier, K.R.; Ellis, D.E.; Marks, L.D. Surface Structures of $SrTiO_3$ (001): A TiO_2-rich Reconstruction with a c (4×2) Unit Cell. *J. Am. Chem. Soc.* **2003**, *125*, 10050–10056. [CrossRef] [PubMed]

3. Chun, H.J.; Lee, Y.; Kim, S.; Yoon, Y.; Kim, Y.; Park, S.C. Surface termination of $BaTiO_3$ (111) single crystal: A combined DFT and XPS study. *Appl. Surf. Sci.* **2022**, *578*, 152018. [CrossRef]

4. Brik, M.G.; Ma, C.G.; Krasnenko, V. First-principles calculations of the structural and electronic properties of the cubic $CaZrO_3$ (001) surfaces. *Surf. Sci.* **2013**, *608*, 146–153. [CrossRef]

5. Sambrano, J.R.; Longo, V.M.; Longo, E.; Taft, C.A. Electronic and structural properties of the (001) $SrZrO_3$ surface. *J. Mol. Struct. THEOCHEM* **2007**, *813*, 49–56. [CrossRef]

6. Piskunov, S.; Eglitis, R.I. First principles hybrid DFT calculations of $BaTiO_3/SrTiO_3$ (001) interface. *Solid State Ion.* **2015**, *274*, 29–33. [CrossRef]

7. Zhao, X.; Selloni, A. Structure and stability of $NaTaO_3$ (001) and $KTaO_3$ (001) surfaces. *Phys. Rev. Mater.* **2019**, *3*, 015801. [CrossRef]

8. Eglitis, R.I.; Kleperis, J.; Purans, J.; Popov, A.I.; Jia, R. *Ab initio* calculations of $CaZrO_3$ (011) surfaces: Systematic trends in polar (011) surface calculations of ABO_3 perovskites. *J. Mater. Sci.* **2020**, *55*, 203–217. [CrossRef]

9. Lazaro, S.D.; Longo, E.; Sambrano, J.R.; Beltrán, A. Structural and electronic properties of $PbTiO_3$ slabs: A DFT periodic study. *Surf. Sci.* **2004**, *552*, 149–159. [CrossRef]

10. Jia, W.; Vikhnin, V.S.; Liu, H.; Kapphan, S.; Eglitis, R.; Usvyat, D. Critical effects in optical response due to charge transfer vibronic excitions and their structure in perovskite-like systems. *J. Lumin.* **1999**, *83*, 109–113. [CrossRef]

11. Gellé, F.; Chirita, R.; Mertz, D.; Rastei, M.V.; Dinia, A.; Colis, S. Guideline to atomically flat TiO_2-terminated $SrTiO_3$ (001) surfaces. *Surf. Sci.* **2018**, *677*, 39–45. [CrossRef]

12. Mesquita, W.D.; Oliveira, M.C.D.; Assis, M.; Ribeiro, R.A.P.; Eduardo, A.C.; Teodoro, M.D.; Marques, G.E.; Júnior, M.G.; Longo, E.; Gurgel, M.F.D.C. Unraveling the relationship between bulk structure and exposed surfaces and its effect on the electronic structure and photoluminescent properties of $Ba_{0.5}Sr_{0.5}TiO_3$: A joint experimental and theoretical approach. *Mater. Res. Bull.* **2021**, *143*, 111442. [CrossRef]

13. Zhang, R.; Hwang, G.S. First-principles mechanistic study of the initial growth of SrO by atomic layer deposition on TiO_2-terminated $SrTiO_3$ (001). *J. Phys. Chem. C* **2020**, *124*, 28116. [CrossRef]

14. Eglitis, R.I.; Purans, J.; Popov, A.I.; Jia, R. Tendencies in ABO_3 perovskite and SrF_2, BaF_2 and CaF_2 bulk and surface *F*-center *ab initio* computations at high symmetry cubic structure. *Symmetry* **2021**, *13*, 1920. [CrossRef]

15. Meng, J.; Lan, Z.Y.; Lin, Q.Y.; Chen, T.; Chen, X.; Wei, X.; Lu, Y.H.; Li, J.X.; Zhang, Z. Cubic-like $BaZrO_3$ nanocrystals with exposed {001}/{011} facets and tuned electronic band structure for enhanced photocatalytic hydrogen production. *J. Mater. Sci.* **2019**, *54*, 1967–1976. [CrossRef]

16. Carlotto, S.; Natile, M.M.; Glisenti, A.; Vittadini, A. Adsorption of small molecules at the cobalt-doped $SrTiO_3$ (001) surface: A first-principles investigation. *Surf. Sci.* **2015**, *633*, 68–76. [CrossRef]

17. Kotomin, E.A.; Piskunov, S.; Zhukovskii, Y.F.; Eglitis, R.I.; Gopejenko, A.; Ellis, D.E. The electronic properties of an oxygen vacancy at ZrO_2-terminated (001) surfaces of a cubic $PbZrO_3$: Computer simulations from the first principles. *Phys. Chem. Chem. Phys.* **2008**, *10*, 4258–4263. [CrossRef]

18. Saghayezhian, M.; Sani, S.M.R.; Zhang, J.; Plummer, E.W. Rumpling and enhanced covalency at the $SrTiO_3$ (001) surface. *J. Phys. Chem. C* **2019**, *123*, 8086–8091. [CrossRef]

19. Eglitis, R.I.; Piskunov, S. First principles calculations of $SrZrO_3$ bulk and ZrO_2-terminated (001) surface *F* centers. *Comput. Condens. Matter* **2016**, *7*, 1–6. [CrossRef]

20. Krainyukova, N.V.; Butskii, V.V. RHEED study of stepped (001) surface of strontium titanate. *Appl. Surf. Sci.* **2004**, *235*, 32–37. [CrossRef]

21. Sokolov, M.; Eglitis, R.I.; Piskunov, S.; Zhukovskii, Y.F. *Ab initio* hybrid DFT calculations of BaTiO$_3$ bulk and BaO-terminated (001) surface *F*-centers. *Int. J. Mod. Phys. B* **2017**, *31*, 1750251. [CrossRef]

22. Mueller, D.N.; Machala, M.L.; Bluhm, H.; Chuech, W.C. Redox activity of surface oxygen anions in oxygen-deficient perovskite oxides during electrochemical reactions. *Nat. Commun.* **2015**, *6*, 6097. [CrossRef] [PubMed]

23. Eglitis, R.I.; Popov, A.I. *Ab initio* calculations for the polar (001) surfaces of YAlO$_3$. *Nucl. Instr. Methods B* **2018**, *434*, 1–5. [CrossRef]

24. Kim, J.S.; Yang, J.H.; Kim, B.K.; Kim, Y.C. Proton conduction at BaO-terminated (001) BaZrO$_3$ surface using density functional theory. *Solid State Ion.* **2015**, *275*, 19–22. [CrossRef]

25. Piskunov, S.; Eglitis, R.I. Comparative *ab initio* calculations of SrTiO$_3$/BaTiO$_3$ and SrZrO$_3$/PbZrO$_3$ (001) heterostructures. *Nucl. Instr. Methods B* **2016**, *374*, 20–23. [CrossRef]

26. Erdman, N.; Poeppelmeier, K.R.; Asta, M.; Warschkow, O.; Ellis, D.E.; Marks, L.D. The structure and chemistry of the TiO$_2$-rich surface of SrTiO$_3$ (001). *Nature* **2002**, *419*, 55–58. [CrossRef]

27. Eglitis, R.I. *Ab initio* hybrid DFT calculations of BaTiO$_3$, PbTiO$_3$, SrZrO$_3$ and PbZrO$_3$ (111) surfaces. *Appl. Surf. Sci.* **2015**, *358*, 556–562. [CrossRef]

28. Maalaoui, A.; Said, O.B.; Akriche, S.T.; Al-Deyab, S.S.; Rzaigui, M. Synthesis, Characterization, Fluorescence and Antibacterial Activity of the Re(VII) Complex [ReO$_3$(phen)(H$_2$PO$_4$)]·H$_2$O. *Z. Für. Nat. B* **2012**, *67*, 1178–1184. [CrossRef]

29. Duan, G.; Chen, L.; Jing, Z.; Luna, P.D.; Wen, L.; Zhang, L.; Xu, J.; Li, Z.; Yang, Z.; Zhou, R. Robust Antibacterial Activity of Tungsten Oxide (WO$_{3-x}$) Nanodots. *Chem. Res. Toxicol.* **2019**, *32*, 1357–1366. [CrossRef]

30. Jeevitha, G.; Abhinayaa, R.; Mangalaraj, D.; Ponpandian, N. Tungsten oxide-graphene oxide (WO$_3$-GO) nanocomposite as an efficient photocatalyst, antibacterial and anticancer agent. *J. Phys. Chem. Solids* **2018**, *116*, 137–147. [CrossRef]

31. Alam, N.N.; Malik, N.A.; Samat, M.H.; Hussin, N.H.; Jaafar, N.K.; Radzwan, A.; Mohyedin, M.Z.; Haq, B.U.; Ali, A.M.M.; Hassan, O.; et al. Underlaying mechanism of surface (001) cubic ATiO$_3$ (A = Pb, Sn) in enhancing thermoelectric performance of thin-film applications using density functional theory. *Surf. Interfaces* **2021**, *27*, 101524. [CrossRef]

32. Enterkin, J.A.; Subramanian, A.K.; Russell, B.C.; Castell, M.R.; Poeppelmeier, K.R.; Marks, L.D. A homologous series of structures on the surface of SrTiO$_3$ (110). *Nat. Mater.* **2010**, *9*, 245–248. [CrossRef] [PubMed]

33. Lin, Y.P.; Isakoviča, I.; Gopejenko, A.; Ivanova, A.; Začinskis, A.; Eglitis, R.I.; D'yachkov, P.N.; Piskunov, S. Time-Dependent Density Functional Theory Calculations of N- and S-Doped TiO$_2$ Nanotube for Water-Splitting Applications. *Nanomaterials* **2021**, *11*, 2900. [CrossRef] [PubMed]

34. Bae, K.; Young, J.D.; Jong, C.H.; Kim, D.; Hong, J.; Kim, B.K.; Lee, J.; Son, J.W.S.; Shim, J.H. Demonstrating the Potential of Yttrium-Doped Barium Zirconate Electrolyte for High-Performance Fuell Cells. *Nat. Commun.* **2017**, *8*, 14553. [CrossRef] [PubMed]

35. Duan, C.; Tong, J.; Shang, M.; Nikodemski, S.; Sanders, M.; Ricote, S.; Almansoori, A.; O'Hayre, R. Readily Processed Protonic Ceramic Fuell Cells with High Performance at Low Temperatures. *Science* **2015**, *349*, 1321–1326. [CrossRef]

36. Duan, C.; Kee, R.; Zhu, H.; Sullivan, N.; Shu, L.; Bian, L.; Jennings, D.; O'Hayre, R. Highly Efficient Reversible Protonic Ceramic Electrochemical Cells for Power Generation and Fuel Production. *Nat. Energy* **2019**, *4*, 230–240. [CrossRef]

37. Choi, S.; Kucharczyk, C.J.; Liang, Y.; Zhang, X.; Takeuchi, I.; Ji, H.I.; Haile, S.M. Exceptional Power Density and Stability at Intermediate Temperature in Protonic Ceramic Fuel Cells. *Nat. Energy* **2018**, *3*, 202–210. [CrossRef]

38. Duan, C.; Kee, R.J.; Zhu, H.; Karakaya, C.; Chen, Y.; Ricote, S.; Jarry, A.; Crumlin, E.J.; Hook, D.; Braun, R.; et al. Highly Durable, Coking and Sulfur Tolerant, Fuel-Flexible Protonic Ceramic Fuel Cells. *Nature* **2018**, *557*, 217–222. [CrossRef]

39. Morendo, S.H.; Zanón, R.; Escolástico, S.; Yuste-Tirados, I.; Malerød-Fjeld, K.; Vestre, P.K.; Coors, W.G.; Martinez, A.; Norby, T.; Serra, J.M.; et al. Direct Conversion of Methane to Aromatics in a Catalytic co-ionic Membrane Reactor. *Science* **2016**, *353*, 563–566.

40. Malerød-Fjeld, K.; Clark, D.; Yuste-Tirados, I.; Zanon, R.; Catalán-Martinez, D.; Beeaff, D.; Morejudo, S.H.; Vestre, P.K.; Norby, T.; Haugsrud, R.; et al. Thermo-Electrochemical Production of Compressed Hydrogen from Methane with Near-Zero Energy Loss. *Nat. Energy* **2017**, *2*, 923–931. [CrossRef]

41. Dawber, M.; Rabe, K.M.; Scott, J.F. Physics of thin-film ferroelectric oxides. *Rev. Mod. Phys.* **2005**, *77*, 1083–1130. [CrossRef]

42. Cohen, R.E. Origin of ferroelectricity in perovskite oxides. *Nature* **1992**, *358*, 136–138. [CrossRef]

43. Zhong, W.; Vanderbilt, D.; Rabe, K.M. Phase Transitions in BaTiO$_3$ from First Principles. *Phys. Rev. Lett.* **1994**, *73*, 1861. [CrossRef] [PubMed]

44. Zhong, W.; Vanderbilt, D.; Rabe, K.M. First-principles theory of ferroelectric phase transitions for perovskites: The case of BaTiO$_3$. *Phys. Rev. B* **1995**, *52*, 6301. [CrossRef] [PubMed]

45. Oliveira, M.C.; Ribeiro, R.A.P.; Longo, E.; Bomio, M.R.D.; Motta, F.V.; Lazaro, S.R.D. Temperature dependence on phase evolution in the BaTiO$_3$ polytypes studied using *ab initio* calculations. *Int. J. Quantum Chem.* **2020**, *120*, e26054. [CrossRef]

46. Meyer, B.; Padilla, J.; Vanderbilt, D. Theory of PbTiO$_3$, BaTiO$_3$ and SrTiO$_3$ surfaces. *Faraday Discuss.* **1999**, *114*, 395–405. [CrossRef]

47. Heifets, E.; Ho, J.; Merinov, B. Density functional simulation of the BaZrO$_3$ (011) surface structure. *Phys. Rev. B* **2007**, *75*, 155431. [CrossRef]

48. Heifets, E.; Kotomin, E.A.; Maier, J. Semi-empirical simulations of surface relaxation for perovskite titanates. *Surf. Sci.* **2000**, *462*, 19–35. [CrossRef]

49. Eglitis, R.I.; Kotomin, E.A.; Borstel, G. Quantum chemical modelling of perovskite solid solutions. *J. Phys. Condens. Matter* **2000**, *12*, L431–L434. [CrossRef]

50. Meyer, B.; Vanderbilt, D. *Ab initio* study of BaTiO$_3$ and PbTiO$_3$ surfaces in external electric fields. *Phys. Rev. B* **2001**, *63*, 205426. [CrossRef]
51. Zhang, J.M.; Pang, Q.; Xu, K.W.; Ji, V. First-principles study of the (110) polar surface of cubic PbTiO$_3$. *Comput. Mater. Sci.* **2009**, *44*, 1360–1365. [CrossRef]
52. Eglitis, R.I.; Purans, J.; Gabrusenoks, J.; Popov, A.I.; Jia, R. Comparative *ab initio* calculation of ReO$_3$, SrZrO$_3$, BaZrO$_3$, PbZrO$_3$ and CaZrO$_3$ (001) surfaces. *Crystals* **2020**, *10*, 745. [CrossRef]
53. Eglitis, R.I.; Purans, J.; Jia, R. Comparative Hybrid Hartree-Fock-DFT Calculations of ReO$_3$, SrTiO$_3$, BaTiO$_3$, PbTiO$_3$ and CaTiO$_3$ (001) Surfaces. *Integr. Ferroelectr.* **2021**, *220*, 9–17. [CrossRef]
54. Eglitis, R.I.; Purans, J.; Jia, R. Comparative Hybrid Hartree-Fock-DFT Calculations of WO$_2$-Terminated Cubic WO$_3$ as well as SrTiO$_3$, BaTiO$_3$, PbTiO$_3$ and CaTiO$_3$ (001) surfaces. *Crystals* **2021**, *11*, 455. [CrossRef]
55. Cora, F.; Stachiotti, M.G.; Catlow, C.R.A. Transition Metal Oxide Chemistry: Electronic Structure of WO$_3$, ReO$_3$ and NaWO$_3$. *J. Phys. Chem. B* **1997**, *101*, 3945–3952. [CrossRef]
56. Weckhuysen, B.M.; Jehng, J.M.; Wachs, I.E. In Situ Raman Spectroscopy of Supported Transition Metal Oxide Catalysts: ^{18}O$_2$-^{16}O$_2$ Isotopic Labeling Studies. *J. Phys. Chem. B* **2000**, *104*, 7382–7387. [CrossRef]
57. Koffyberg, F.P.; Dwight, K.; Wold, A. Interband transitions of semiconducting oxides determined from photoelectrolysis spectra. *Solid State Commun.* **1979**, *30*, 433–437. [CrossRef]
58. Wemple, S.H. Polarized Fluctuations and the Optical-Absorption Edge in BaTiO$_3$. *Phys. Rev. B* **1970**, *2*, 2679–2689. [CrossRef]
59. Benthem, K.; Elsässer, C.; French, R.H. Bulk electronic structure of SrTiO$_3$: Experiment and Theory. *J. Appl. Phys.* **2001**, *90*, 6156–6164. [CrossRef]
60. Robertson, J. Band offsets of wide-band-gap oxides and implications for future electronic devices. *J. Vacuum. Sci. Technol. B* **2000**, *18*, 1785–1791. [CrossRef]
61. Schirber, J.E.; Morosin, B. "Compressibility Collapse" Transition in ReO$_3$. *Phys. Rev. Lett.* **1979**, *42*, 1485–1487. [CrossRef]
62. Balászi, C.; Farkas-Jahnke, M.; Kotsis, I.; Petrás, L.; Pfeifer, J. The observation of cubic tungsten trioxide at high-temperature dehydration of tungstic acid hydrate. *Solid State Ion.* **2001**, *141–142*, 411–416. [CrossRef]
63. Edwards, J.W.; Speiser, R.; Johnston, H.L. Structure of Barium Titanate at Elevated Temperatures. *J. Am. Chem. Soc.* **1951**, *73*, 2934–2935. [CrossRef]
64. Okazaki, A.; Scheel, H.J.; Müller, K.A. The lattice constant vs. temperature relation around the 105 K transition of a flux-grown SrTiO$_3$ crystal. *Phase Trans.* **1985**, *5*, 207–218.
65. Mathews, M.D.; Mirza, E.B.; Momin, A.C. High-temperature X-ray diffractometric studies of CaZrO$_3$, SrZrO$_3$ and BaZrO$_3$. *J. Mater. Sci. Lett.* **1991**, *10*, 305–306. [CrossRef]
66. Perdew, J.P.; Wang, Y. Accurate and simple density functional for the electronic exchange energy: Generalized gradient approximation. *Phys. Rev. B* **1989**, *33*, 8800–8802; Erratum in *Phys. Rev. B* **1989**, *40*, 3399. [CrossRef]
67. Perdew, J.P.; Wang, Y. Accurate and simple analytic representation of the electron-gas correlation energy. *Phys. Rev. B* **1992**, *45*, 13244–13249. [CrossRef]
68. Lee, C.; Yang, W.; Parr, R.G. Development of the Colle-Salvetti correlation-energy formula into a functional of the electron density. *Phys. Rev. B* **1988**, *37*, 785–789. [CrossRef]
69. Saunders, V.R.; Dovesi, R.; Roetti, C.; Causa, N.; Harrison, N.M.; Orlando, R.; Zicovich-Wilson, C.M. *CRYSTAL-2009 User Manual*; University of Torino: Torino, Italy, 2009.
70. Monkhorst, H.J. Special points for Brillouin-zone integrations. *Phys. Rev. B* **1976**, *13*, 5188. [CrossRef]
71. Piskunov, S.; Heifets, E.; Eglitis, R.I.; Borstel, G. Bulk properties and electronic structure of SrTiO$_3$, BaTiO$_3$, PbTiO$_3$ perovskites: An *ab initio* HF/DFT study. *Comput. Mater. Sci.* **2004**, *29*, 165–178. [CrossRef]
72. Piskunov, S.; Kotomin, E.A.; Heifets, E.; Maier, J.; Eglitis, R.I.; Borstel, G. Hybrid DFT calculations of the atomic and electronic structure for ABO$_3$ perovskite (001) surfaces. *Surf. Sci.* **2005**, *575*, 75–88. [CrossRef]
73. Eglitis, R.I.; Popov, A.I. Systematic trends in (001) surface *ab initio* calculations of ABO$_3$ perovskites. *J. Saudi Chem. Soc.* **2018**, *22*, 459–468. [CrossRef]
74. Vassilyeva, A.F.; Eglitis, R.I.; Kotomin, E.A.; Dauletbekova, A.K. *Ab initio* calculations of MgF$_2$ (001) and (011) surface structure. *Phys. B Condens. Matter* **2010**, *405*, 2125–2127. [CrossRef]
75. Rubloff, G.W. Far-Ultraviolet Reflectence Spectra and the Electronic Structure of Ionic Crystals. *Phys. Rev. B* **1972**, *5*, 662–684. [CrossRef]
76. Lisitsyn, V.M.; Lisitsyna, L.A.; Popov, A.I.; Kotomin, E.A.; Abuova, F.U.; Akilbekov, A.; Maier, J. Stabilization of primary mobile radiation defects in MgF$_2$ crystals. *Nucl. Instrum. Methods B* **2016**, *374*, 24–28. [CrossRef]
77. Slater, J.C. A Simplification of the Hartree-Fock Method. *Phys. Rev.* **1951**, *81*, 385–390. [CrossRef]
78. Dovesi, R.; Orlando, R.; Roetti, C.; Pisani, C.; Saunders, V.R. The Periodic Hartree-Fock Method and Its Implementation in the Crystal Code. *Phys. Stat. Sol. B* **2000**, *217*, 63–88. [CrossRef]
79. Dirac, P.A.M. Note on Exchange Phenomena in the Thomas Atom. *Proc. Camb. Phil. Soc.* **1930**, *26*, 376–385. [CrossRef]
80. Vosko, S.H.; Wilk, L.; Nusair, M. Accurate spin-dependent electron liquid correlation energies for local spin density calculations: A critical analysis. *Can. J. Phys.* **1980**, *58*, 1200–1211. [CrossRef]
81. Press, W.H.; Teukolsky, S.A.; Vetterling, W.T.; Flannery, B.P. *Numerical Recipes in Fortran 77*, 2nd ed.; Cambridge University Press: Cambridge, MA, USA, 1997.

82. Noguera, C. Polar oxide surfaces. *J. Phys. Condens. Matter* **2000**, *12*, R367. [CrossRef]
83. Pojani, A.; Finocchi, F.; Noguera, C. Polarity on the $SrTiO_3$ (111) and (110) surfaces. *Surf. Sci.* **1999**, *442*, 179–198. [CrossRef]
84. Pojani, A.; Finocchi, F.; Noguera, C. A theoretical study of the unreconstructed polar (111) face of $SrTiO_3$. *Appl. Surf. Sci.* **1999**, *142*, 177–181. [CrossRef]
85. Cora, F.; Patel, A.; Harrison, N.M.; Dovesi, R.; Catlow, C.R.A. An *ab initio* Hartree-Fock study of the cubic and tetragonal phases of bulk tungsten trioxide. *J. Am. Chem. Soc.* **1996**, *118*, 12174–12182. [CrossRef]
86. Mayer, I. Bond Order and Valence: Relations to Mulliken's Population Analysis. *Int. J. Quantum Chem.* **1984**, *26*, 151–154. [CrossRef]
87. Bochicchio, R.C.; Reale, H.F. On the nature of crystalline bonding: Extension of statistical population analysis to two- and three-dimensional crystalline systems. *J. Phys. B* **1993**, *26*, 4871–4883. [CrossRef]
88. Shi, H.; Chang, L.; Jia, R.; Eglitis, R.I. *Ab initio* calculations of the transfer and aggregation of *F* centers in CaF_2. *J. Phys. Chem. C* **2012**, *116*, 4832–4839. [CrossRef]
89. Grigorjeva, L.; Millers, D.K.; Pankratov, V.; Williams, R.T.; Eglitis, R.I.; Kotomin, E.A. Experimental and theoretical studies of polaron optical properties in $KNbO_3$ perovskites. *Solid State Commun.* **2004**, *129*, 691–696. [CrossRef]
90. Eglitis, R.I. Comparative First-Principles Calculations of $SrTiO_3$, $BaTiO_3$, $PbTiO_3$ and $CaTiO_3$ (001), (011) and (111) Surfaces. *Ferroelectrics* **2015**, *483*, 53–67. [CrossRef]
91. Eglitis, R.I.; Vanderbilt, D. *Ab initio* calculations of $BaTiO_3$ and $PbTiO_3$ (001) and (011) surface structures. *Phys. Rev. B* **2007**, *76*, 155439. [CrossRef]
92. Eglitis, R.I.; Vanderbilt, D. First-principles calculations of atomic and electronic structure of $SrTiO_3$ (001) and (011) surfaces. *Phys. Rev. B* **2008**, *77*, 195408. [CrossRef]
93. Eglitis, R.I. First-principles calculations of $BaZrO_3$ (001) and (011) surfaces. *J. Phys. Condens. Matter* **2007**, *19*, 356004. [CrossRef]
94. Padilla, J.; Vanderbilt, D. *Ab initio* study of $SrTiO_3$ surfaces. *Surf. Sci.* **1998**, *418*, 64–70. [CrossRef]
95. Cheng, C.; Kunc, K.; Lee, M.H. Structural relaxation and longitudinal dipole moment of $SrTiO_3$ (001) (1×1) surfaces. *Phys. Rev. B* **2000**, *62*, 10409. [CrossRef]
96. Bickel, N.; Schmidt, G.; Heinz, K.; Müller, K. Ferroelectric relaxation of the $SrTiO_3$ (100) surface. *Phys. Rev. Lett.* **1993**, *62*, 2009–2012. [CrossRef]
97. Hikita, T.; Hanada, T.; Kudo, M.; Kawai, M. Structure and electronic state of the TiO_2 and SrO terminated $SrTiO_3$ (100) surfaces. *Surf. Sci.* **1993**, *287–288*, 377–381. [CrossRef]
98. Charlton, G.; Brennan, S.; Muryn, C.A.; McGrath, R.; Norman, D.; Turner, T.S.; Thorthon, G. Surface relaxation of $SrTiO_3$ (001). *Surf. Sci.* **2000**, *457*, L376–L380. [CrossRef]